A sharp-interface treatment technique for two-phase flows in meshless methods

Yan Zhou*

School of Engineering, University of Liverpool

*Corresponding author email: yan.zhou@liverpool.ac.uk

Abstract

In this paper, a new interface treatment technique for multi-phase meshless methods is proposed. It enables the interface conditions to be applied effectively on the interface points in two-phase flows involving interface tension and high viscosity. This technique is incorporated in the Meshless Local Petrov-Galerkin method with the Rankine source solution (MLPG_R) and the model predictions are validated through a number of standard test cases. Convergent results that agreed well with both available analytical and numerical solutions from other methods are obtained in simulations of square-droplet deformation, capillary wave, bubble rising and Rayleigh-Taylor instability. In these cases, sharp pressure discontinuity at the interface is well predicted with depressed parasitic current and the capability of the technique in dealing with high viscosity is comprehensively demonstrated.

Keywords: meshless method; two-phase flow; sharp interface; interface tension; high viscosity

1. Introduction

Two-phase flow where clear interfaces separate different fluids due to discontinuities of fluid properties across the interface exists both in nature and in a wide range of industrial processes. Many applications such as water dripping from a nozzle, formation of bubbles and liquid sprays involve significant effects of interface tension and viscosity. Interface tension and viscous force can even be the dominant forces in many commonly occurring two-phase flows such as deformation of fluid drops in viscous fluids or capillary waves [1,2]. From the numerical perspective, the former involves a singular stress that acts only at the interface while the latter is characterised by the discontinuity of high viscosity, both of which need to be properly formulated in the interface treatment using either mesh-based method with an Eulerian or arbitrary Eulerian-Lagrangian formulation or meshless methods based on a Lagrangian formulation.

In mesh-based methods, interface is commonly captured by volume of fluid (VOF) [3,4] or level set methods [5,6], in which fluid properties are continuously transferred within the interface region. The interface tension is generally computed by the continuous surface force (CSF) method [7]. The singular surface tension in the CSF method is regularized to a volumetric surface force spreading within the interface region. However, the artificial mixing region and artificial spreading of the interface tension may generate unphysical parasitic currents near the interface [8,9]. Fully coupled treatments of interface tension singularity were achieved by Sussman et al. [10] using the ghost fluid method [11] to handle the pressure jump. With the density and viscosity being defined at the mesh face according to the reconstructed interface segment, Luo et al. [12] achieved the sharp interface and full coupling by integrating extra interfacial momentum flux and ensuring the shear stress continuity at the sub-grid reconstructed interface. Arbitrary Lagrangian Eulerian (ALE) methods [13] were developed in which the interface is represented by mesh faces which move with the flow and the sharply separated phases ensure that each mesh is occupied by only one phase of fluids. The interface conditions including pressure jump and velocity continuity are explicitly enforced at the infinitely thin interface through extensive and time consuming mesh adaption and regeneration.

With meshless methods the interface is inherently advected by Lagrangian moving particles without involving complex interface capturing algorithms. By assigning each particle to a single phase throughout the simulation, interface even with large deformation or breakup can be followed in a straightforward manner. Among the established meshless methods, both Smoothed Particle Hydrodynamics (SPH) [14-17] and Moving Particle Semi-implicit (MPS) [18,19] methods have shown their remarkable flexibility in handling multiphase flows involving large density and viscosity ratio and interface tension.

There are mainly two categories of approaches to dealing with interface conditions in meshless methods, one of which is one-fluid category without explicit implementation of the interface conditions. With this approach, for either SPH [20,21] or MPS [18,19], a smoothing scheme involving a spatially weighted averaging is usually adopted to continuously transfer fluid density and viscosities across the interface. However, it has been pointed out that such smoothing schemes may have problems of satisfying mass conservation [2] and may also result in unphysical diffusion, i.e. unphysical particle dispersion at the interface [19]. Effort has been made to develop a higher order density smoothing scheme [19] so as to achieve more accurate and sharper density reconstruction at the interface or to maintain the density discontinuity by considering volume rather than mass of neighbouring particles [2,22]. Harmonic mean viscosity is another alternative for viscosity treatment near the interface which is also in wide applications [2,17,20]. It is noted that all those density and viscosity treatments for multiphase flow simulations are also accompanied by various discretized operators either for gradients or Laplacians [2,19].

The other category seeks to track the interface movement by explicitly imposing interface conditions with respect to the pressure (p) and the ratio of pressure gradient to density ($\frac{\nabla p}{\rho}$). Three such interface conditions have been implemented into meshless methods to simulate multiphase flows, namely (1) continuous p and $\frac{\nabla p}{\rho}$ [14], (2) continuous p only [23] and (3) continuous p with a specified $\frac{\nabla p}{\rho}$ jump [24]. Hu and Adams [14] implemented the first condition into the inter-particle-averaged derivatives to formulate specific gradient and Lapacian operators for pressure near the interface. As the interface is assumed to locate at the middle of each pair of particles belonging to different phases, the two conditions are applied on an interface with a thickness depending on the kernel smoothing length. Shao [23] implemented the second condition but considered an infinitely thin interface ignoring either the kinematic interface condition or the interface tension. The method is therefore limited to flows with relatively low density ratios (up to 1.3). Lind et al. [25] also imposed the condition of pressure continuity to solve incompressible water phase and the velocity continuity condition to solve compressible air phase. Interface tension was not considered. Recently Zhou et al. [24] proposed an interface implementation method that enforces the third condition at an infinitely thin interface. For the case of low viscosity when an averaged viscous force can be applied at the interface and in the absence of interface tension, p and $\frac{\nabla p}{\rho}$ could be simplified to be continuous and were implemented in the meshless local Petrov-Galerkin method based on the Rankine source solution (MLPG_R). Through a number of validation tests the model was found to have second-order convergence and is accurate for the density ratio ranging from 1 to 1000.

In meshless methods considering interface tension, the continuous surface force (CSF) method is generally employed, by adding a body force reformulated from the interface tension stress in the momentum equation [7] and distributing this body force over a layer of particles predefined as the interface [20,26,27]. The curvature for CSF is calculated either as the second order derivative of the phase indicator function or derived analytically from reconstructed interface curve [28]. Continuous Surface Stress (CSS) taking first order derivative of the indicator was also implemented in the multiphase SPH models [2]. For CSF and CSS interface tension schemes, instead of predicting a sharp pressure jump at the interface, continuous pressure variations are obtained as the singular stress is taken to be continuous over a certain length across the sharp interface.

In this study, a new interface treatment technique for multi-phase meshless methods is presented. As an extension of the previous work [24] the technique is formulated using MLPG_R method [29]. The interface treatment prescribes specific jumps in both p and $\frac{\nabla p}{\rho}$ which are derived from normal stress balance and continuous velocity at the interface including the effects of interface tension and high viscosity. The consideration of the interface tension is achieved by a sharp pressure jump at the interface rather than the conventional continuous scheme. A number of numerical tests involving square-droplet deformation, capillary wave, rising bubble and Rayleigh-Taylor instability are carried out to demonstrate the potential of the present method in determining the effects of surface tension and handling high viscosity. The results show that sharp pressure jump at the interface is well maintained and the parasitic current is depressed. The capillary wave case shows an approximate second order convergent rate as compared to the analytical solution. In the case of rising bubble a smooth terminal shape under the action of high interface tension and high viscosity is obtained. Both calculated rising velocity and centroid position compared well with the simulation results using mesh-based numerical methods. The simulation of Rayleigh-Taylor instability shows an accurate instability growth and a clear separation of phases for complex interface profiles in a long time simulation.

2. Governing equations and computational procedures

The governing equations are the incompressible Navier-Stokes equations in Lagragian formalism for two immiscible fluids.

$$\frac{d\vec{u}_\alpha}{dt} = \vec{g} - \frac{1}{\rho_\alpha}\nabla p_\alpha + \upsilon_\alpha \nabla^2 \vec{u}_\alpha \tag{1}$$

$$\nabla \cdot \vec{u}_\alpha = 0 \tag{2}$$

where $\vec{g}$ is the gravitational acceleration, $\vec{u}_\alpha$ is the particle velocity vector for fluid phase α, p is the pressure, ρ is the fluid density and υ is the fluid kinematic viscosity. The subscript $\alpha = l, k$ presents the two phases that particles belong to. As for surface tension (referring to interface tension between two immiscible phases in this paper), unlike other meshless methods treating the interface tension as a volumetric force and adding a term on the right hand side of Eq. (1) [10,12,20,22], the treatment in this paper will be based on the normal stress condition at the interface and so the surface tension appears in the interface conditions, which will be detailed in the next section.

The projection method is used to solve pressure and velocity field as in many meshless simulations for incompressible fluids [30-32]. In this method both the density and mass of particles are assumed to be constant. Based on the known variables of each particle at n-th time step ($t = t^n$), an intermediate velocity ${\vec{u}_\alpha}^*$is firstly calculated according to Eq. (1) without the pressure gradient term.

$${\vec{u}_\alpha}^* = {\vec{u}_\alpha}^n + \vec{g}\Delta t + \upsilon_\alpha \nabla^2 \vec{u}_\alpha \Delta t \tag{3}$$

The pressure at $t^{n+1}$is obtained from solving the pressure Poisson's equation (PPE),

$$\nabla^2 {p_\alpha}^{n+1} = \frac{\rho_\alpha}{\Delta t} \nabla \cdot {\vec{u}_\alpha}^* \tag{4}$$

The particle velocities and positions at $t^{n+1}$are then updated by

$$\vec{u}_{\alpha}{}^{n+1} = \vec{u}_{\alpha}{}^{*} - \frac{\Delta t}{\rho_{\alpha}} \nabla p_{\alpha}{}^{n+1} \tag{5}$$

$$\vec{r}_{l}{}^{n+1} = \vec{u}_{l}{}^{n} + \vec{u}_{l}{}^{n+1} \Delta t \tag{6}$$

To solve the PPE within each phase, MLPG_R method will be adopted to obtain a weak formulation of Eq. (4) by integrating the equation , details of which can be found in Ma and Zhou [33].

3. Interface conditions

In the previous work [24], interface conditions for small viscosity and zero interface tension were presented which impose the continuity in pressure, and continuous normal velocity at the interface particles. To deal with fluids with interface tension and high viscosities, the interface conditions [7,10] adopted here are continuity condition for velocity,

$$\vec{u}_{l} = \vec{u}_{k} \tag{7}$$

continuity condition for normal stress

$$p_{l} - p_{k} = \tau_{l,n} - \tau_{k,n} + \sigma \kappa \tag{8}$$

and continuity condition for tangential stress

$$\tau_{l,\tau} = \tau_{k,\tau} \tag{9}$$

where σ is a constant interface tension coefficient, κ is the curvature and the sign of the surface tension indicates that phase l is on the convex side. $\tau_{l,n}$ and $\tau_{k,n}$ are normal viscous stresses on two sides of the interface, $\tau_{l,\tau}$ and $\tau_{k,\tau}$ are tangential viscous stress, which can be expressed by

$$\tau_{\alpha,n} = 2\mu_{\alpha} n_{j} \left(\frac{\partial u_{j}}{\partial n} \right)$$

$$\tau_{\alpha,\tau} = \mu_{\alpha} \left[n_{j} \left(\frac{\partial u_{j}}{\partial \tau} \right) + \tau_{j} \left(\frac{\partial u_{j}}{\partial n} \right) \right] \quad j = 1,2$$

where $\vec{n} = (n_1, n_2)$ and $\vec{\tau} = (\tau_1, \tau_2)$ are the unit normal and tangent respectively to the interface. Eq. (8) implies that p is discontinuous when normal viscous stress or interface tension is taken into consideration. The interface tension may also be considered by other approaches in meshless method such as CSF in Zainali et al. [20] and CSS in Hu and Adams [2]. But in both approaches, rather than treating it in the interface condition as Eq. (8), the interface tension is converted to a volumetric force and is added to the RHS of the momentum equation. The continuity of tangential stress is imposed in the calculation of the intermediate velocity following the procedure proposed by Shao [23] involving the update of the tangential stress at the interface in one phase using the value of the corresponding tangential stress in the other phase.

3.1 *Derivation of discontinuous* $\frac{\nabla p}{\rho}$

To solve PPE for each phase, conditions associated with pressure at the interface need to be provided. In addition to the usual pressure jump condition (i.e. Eq. (8)), a condition containing pressure gradient can be derived. In the Lagrangian formulation, the continuous velocity across the interface implies that the particle acceleration at the interface is continuous as well as [34], which can be expressed as.

$$\frac{d\vec{u}_l}{dt} = \vec{F}_u = \vec{g} - \frac{1}{\rho_l}\nabla p_l + \upsilon_l \nabla^2 u_l \qquad (10)$$

$$\frac{d\vec{u}_k}{dt} = \vec{F}_u = \vec{g} - \frac{1}{\rho_k}\nabla p_k + \upsilon_k \nabla^2 u_k \qquad (11)$$

where $\vec{F}_u$ denotes the matched particle acceleration for each phase at the interface. Rearranging Eqs. (10) and (11), the expressions of $\frac{\nabla p}{\rho}$ for each phase can be obtained.

$$\left(\frac{\nabla p}{\rho}\right)_l = \vec{g} - \vec{F}_u + \upsilon_l \nabla^2 \vec{u}_l \qquad (12)$$

$$\left(\frac{\nabla p}{\rho}\right)_k = \vec{g} - \vec{F}_u + \upsilon_k \nabla^2 \vec{u}_k \qquad (13)$$

For fluids with zero or very low viscosities, $\upsilon_\alpha \nabla^2 \vec{u}_\alpha$ in Eq. (12) and (13) may be replaced by the averaging value of $(\upsilon_l \nabla^2 \vec{u}_l + \upsilon_k \nabla^2 \vec{u}_k)/2$ as proposed in Zhou et al. [24]. With that averaging, the jump of $\frac{\nabla p}{\rho}$ can be eliminated by imposing the velocity continuity at the interface, representing as $\left[\frac{\nabla p}{\rho}\right]_{LV} = 0$. Continuous $\frac{\nabla p}{\rho}$ condition was also used to approximate inter-particle averaged derivatives in SPH together with the viscous force derived from the inter-particle-averaged stress [14,27]. However, for high viscous fluids separated by a sharp interface, averaging the viscous term as in Zhou et al. [24] is no longer feasible and the viscous term needs to be considered separately for each phase without introducing any artificial smoothing. By subtracting Eq. (13) from Eq. (12), it yields

$$\left(\frac{\nabla p}{\rho}\right)_l - \left(\frac{\nabla p}{\rho}\right)_k = \upsilon_l \nabla^2 \vec{u}_l - \upsilon_k \nabla^2 \vec{u}_k \tag{14}$$

Eq. (14) gives the jump in pressure gradient over density for high viscous fluids, abbreviated as$\left[\frac{\nabla p}{\rho}\right]_{HV}$. Numerical tests will be carried out to compare the capability of $\left[\frac{\nabla p}{\rho}\right]_{HV}$ and $\left[\frac{\nabla p}{\rho}\right]_{LV}$ in handling fluids with various viscosities in section 4.2.

3.2 *Interface Pressure formulation*

The pressure near the interface will be derived by combining the jump conditions of p and $\frac{\nabla p}{\rho}$ given by Eqs. (8) and (14). The pressure of each phase near the interface particles is firstly expanded into a Taylor series:

$$\frac{1}{\rho_l}\left(p_l(\vec{r}_l) - p_l(\vec{r}_0)\right) = \frac{1}{\rho_l}(\nabla p_l)_{\vec{r}_0} \cdot (\vec{r}_l - \vec{r}_0) + O(|\vec{r}_l - \vec{r}_0|^2) \tag{15}$$

$$\frac{1}{\rho_k}\left(p_k(\vec{r}_k) - p_k(\vec{r}_0)\right) = \frac{1}{\rho_k}(\nabla p_k)_{\vec{r}_0} \cdot (\vec{r}_k - \vec{r}_0) + O(|\vec{r}_k - \vec{r}_0|^2) \tag{16}$$

where $p_l(\vec{r}_l)$ and $p_k(\vec{r}_k)$ are pressures in phase l and k respectively at arbitrary point of $\vec{r}$ while $p_l(\vec{r}_0)$ and $p_k(\vec{r}_0)$ are these for $\vec{r}$ tending to $\vec{r}_0$from both sides of the interface with $\vec{r}_0$ being the positon vector of the interface. Discretising Eq. (15) and (16) in the support domain within each phase and substituting the jump condition of Eq. (14) yield

$$\begin{aligned} &\frac{1}{\rho_l}\sum_{j=1}^{n}\left(p_l(r_j) - p_l(r_0)\right)\emptyset_l(r_{j0}) \\ &\qquad = \left[\upsilon_l \nabla^2 \vec{u}_l - \upsilon_k \nabla^2 \vec{u}_k + \left(\frac{\nabla p}{\rho}\right)_k\right]_{r_0} \cdot \sum_{j=1}^{n}(\vec{r}_j - \vec{r}_0)\emptyset_l(\vec{r}_{j0}) \end{aligned} \tag{17}$$

$$\frac{1}{\rho_k}\sum_{q=1}^{m}\left(p_k(r_q)-p_k(r_0)\right)\emptyset_k(r_{q0}) \\ =\left[\left(\frac{\nabla p}{\rho}\right)_k\right]_{r_0}\cdot\sum_{q=1}^{m}(\vec{r}_q-\vec{r}_0)\emptyset_k(\vec{r}_{q0}) \tag{18}$$

where the shape function $\emptyset(\vec{r})$ is obtained by the moving least square (MLS) algorithm [29] with a support domain containing both phases; $\vec{r}_j$ and $\vec{r}_q$ are position vectors of neighbouring particles in phase l and k; n and m are total numbers of neighbouring particles in phase l and k.

Adding up Eq. (17) and (18) and replacing the pressure gradient term according to Eq. (13), it yields

$$\frac{1}{\rho_l}\sum_{j=1}^{n}p_l(\vec{r}_j)\emptyset_l(\vec{r}_{j0})+\frac{1}{\rho_k}\sum_{q=1}^{m}p_k(\vec{r}_q)\emptyset_k(\vec{r}_{q0}) \\ -\left[\frac{p_l(\vec{r}_0)}{\rho_l}\sum_{j=1}^{n}\emptyset_l(\vec{r}_{j0})+\frac{p_k(\vec{r}_0)}{\rho_k}\sum_{q=1}^{m}\emptyset_k(\vec{r}_{q0})\right] \\ =(\vec{g}-\vec{F}_u)_{\vec{r}_0}\left[\sum_{j=1}^{n}(\vec{r}_j-\vec{r}_0)\emptyset_l(\vec{r}_{j0})+\sum_{q=1}^{m}(\vec{r}_q-\vec{r}_0)\emptyset_k(\vec{r}_{q0})\right]+F_v \tag{19}$$

where $F_v=(\upsilon_l\nabla^2\vec{u}_l)_{\vec{r}_0}\cdot\sum_{j=1}^{n}(\vec{r}_j-\vec{r}_0)\emptyset_l(\vec{r}_{j0})+(\upsilon_k\nabla^2\vec{u}_k)_{\vec{r}_0}\cdot\sum_{q=1}^{m}(\vec{r}_q-\vec{r}_0)\emptyset_k(\vec{r}_{q0})$.

Although the first term of the RHS of Eq. (19) can be omitted when sufficient particles are used, it will be retained as $F_r{}'$ hereafter to cover the situations of insufficient or unevenly distributed particles. $F_r{}'$ is computed by the parameters obtained from the previous time step.

The explicit pressure expression for interface particles is then obtained by rearranging Eq. (19) and utilising the pressure jump in Eq. (8) showing as

$$p_k(\vec{r}_0)=\frac{\frac{1}{\rho_l}\sum_{j=1}^{n}p_l(\vec{r}_j)\emptyset_l(\vec{r}_{j0})+\frac{1}{\rho_k}\sum_{q=1}^{m}p_k(\vec{r}_q)\emptyset_k(\vec{r}_{q0})-F_r{}'-F_v-F_{n,k}}{\frac{1}{\rho_l}\sum_{j=1}^{n}\emptyset_l(\vec{r}_{j0})+\frac{1}{\rho_k}\sum_{q=1}^{m}\emptyset_k(\vec{r}_{q0})} \tag{20}$$

$$p_l(\vec{r}_0)=\frac{\frac{1}{\rho_l}\sum_{j=1}^{n}p_l(\vec{r}_j)\emptyset_l(\vec{r}_{j0})+\frac{1}{\rho_k}\sum_{q=1}^{m}p_k(\vec{r}_q)\emptyset_k(\vec{r}_{q0})-F_r{}'-F_v+F_{n,l}}{\frac{1}{\rho_l}\sum_{j=1}^{n}\emptyset_l(\vec{r}_{j0})+\frac{1}{\rho_k}\sum_{q=1}^{m}\emptyset_k(\vec{r}_{q0})} \tag{21}$$

where

$$F_{n,k} = \frac{1}{\rho_l}\left(\tau_{l,n} - \tau_{k,n} + \sigma\kappa\right)\sum_{j=1}^{n} \emptyset_l\left(\vec{r}_{j0}\right)$$

$$F_{n,l} = \frac{1}{\rho_k}\left(\tau_{l,n} - \tau_{k,n} + \sigma\kappa\right)\sum_{q=1}^{m} \emptyset_k\left(\vec{r}_{q0}\right)$$

The pressures expressed by Eqs. (20) and (21) are implemented on each single interface particle and represent the pressures for the phase k and l respectively providing the Dirichlet boundary condition for the solution of pressure Poisson's equation of the each phase. To impose the condition, interface particles are identified based on the absolute density gradient method recently proposed by Zhou and Ma [35]. The terms of F_v and $F_{n,l}$ (or $F_{n,k}$) are generated by the jump of $\frac{\nabla p}{\rho}$ as shown in Eq. (14) and normal stress jump (includes interface tension) respectively. Similarly, explicit pressure expression to provide Dirichlet condition at the interface was also achieved in Shao [23] and Lind et al. [25]. The former ensured the stress balance without considering the interface tension or velocity continuity at the interface. While the latter was proposed for air-water flow ensuring the pressure continuity for the water phase (negligible interface tension and viscosity) and the velocity continuity was implemented individually for the air phase.

3.3 Interface curvature

The surface tension term $\sigma\kappa$ in both Eqs. (20) and (21) is crucial to achieve an accurate pressure jump and consequently the whole pressure field. For existing surface tension model, e.g. CSF [7] and GFM [11], calculations are based on the assumption that the interface is known a priori and the curvature needs to be carefully treated. In the mesh based group, it is widely estimated from an indicator function which can be either a discontinuous fluid distribution function or developed to be smoothed [1,36]. To improve the performance on mesh refinement convergence, an indicator function based on least square approach [37] and height function approach [38] were proposed, achieving first and second order convergence respectively.

For meshless approaches, CSF is also widely adopted for surface tension implementation and the curvature is computed as the divergence of unit normal using an indicator function [2,27]. A method locally reconstructing the interface in conjunction with the interface particle identification was adopted in Zhang et al. [28] in which polynomial or MLS algorithm is used to fit the local interface curve. For the present MLPG_R multiphase model, as the interface is automatically traced by identifying interface particles, local interface curve reconstruction will be used. MLS fitting is used to avoid oscillations that might be caused by polynomial fitting due to disordered interface particle distribution, with details provided in the Appendix.

The curvature obtained by above technique is tested on different types of curves including a circle, $x^2 + y^2 = 1$, an ellipse, $\left(\frac{x}{2}\right)^2 + y^2 = 1$, and a sinusoidal curve, $y = sin(x)$. Particle distances of 0.167, 0.1, 0.063, 0.05, 0.033, 0.02 and 0.013 are tested for the three curves and the L^2 relative errors defined by $E_{L^2} = \sqrt{\frac{\sum_{i=1}^{N}(\kappa_i - \kappa_{ia})^2}{\sum_{i=1}^{N}\kappa_{ia}{}^2}}$ are plotted in Fig. 1, where κ_{ia} is the analytical curvature for the particle on the curve and κ_i is the corresponding numerical curvature. One can observe that second-order convergence is achieved by the local curve fitting with second-order MLS algorithm.

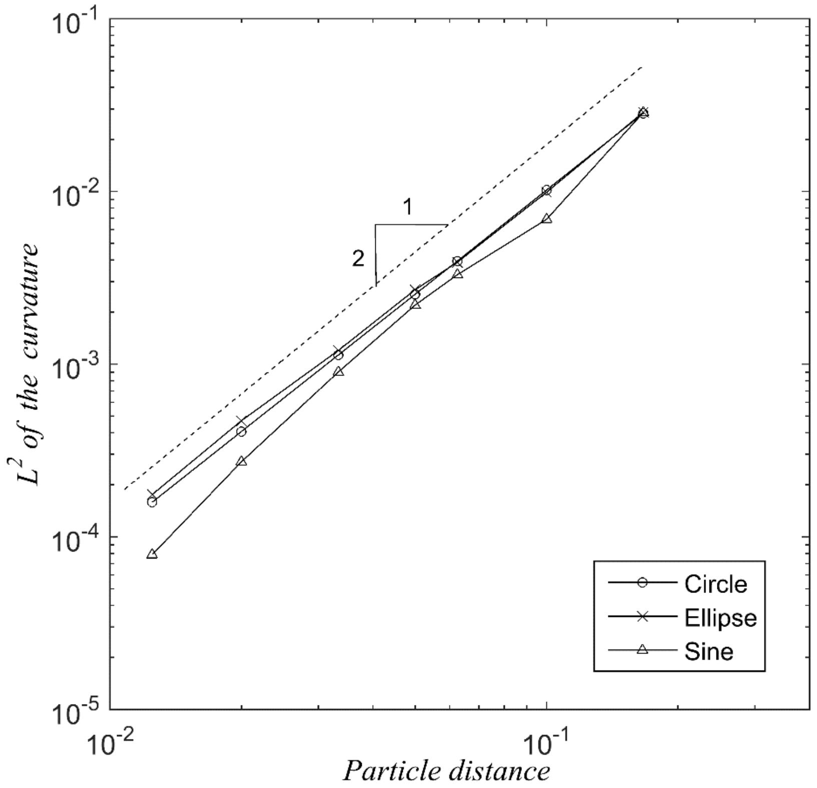

Fig. 1: L^2 errors of curvatures for the circle, ellipse and sine-curve corresponding to different particle distances. The dashed line indicates the second order convergence.

4. Validation results

In this section, a number of numerical experiments involving fluids with interface tension and high viscosity are presented to demonstrate the performance of the method proposed, i.e. the combined implementation of the sharp pressure jump at the interface and the precise determination of interface curvature based on MLS fitting of local interface curve while satisfying the velocity continuity condition, in both normal and tangential directions. Validations are also carried out for the newly derived discontinuous $\left[\frac{\nabla p}{\rho}\right]_{HV}$, Eq. (14), and its corresponding pressure expressions, Eqs. (20) and (21), showing its applicability for high viscous fluids.

4.1 Square-droplet deformation

In this case, an initially squared fluid droplet with density of ρ_1 and dynamic viscosity of μ_1 is located at the centre of a larger square as shown in Fig. 2. The density of the fluid surrounding the inner square is ρ_2 and the viscosity is μ_2. Due to unbalanced surface tension force, capillary waves are induced to oscillate the inner fluid about its equilibrium shape which is a circle based on the Laplace law [39]. Viscous effects damp the oscillation and lead the droplet to its final equilibrium shape.

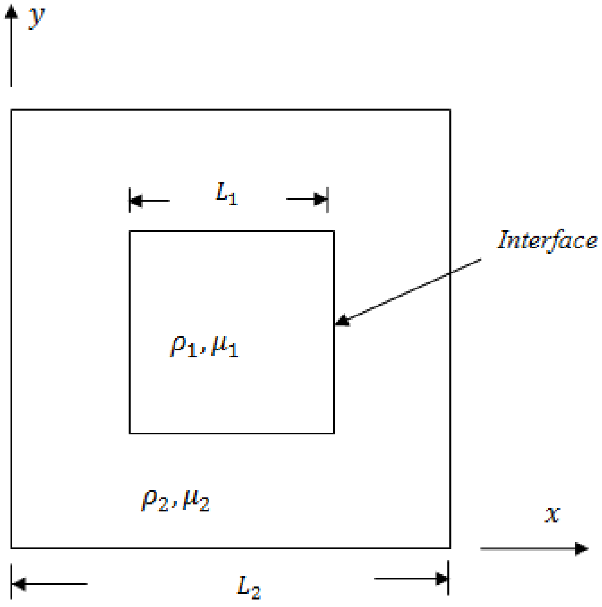

Fig. 2: Setup of square-droplet deformation test

In the tests on the same case previously carried out to validate surface tension models and interface curvature estimations [7,27,28,36], the unphysical residual flows at latter equilibrium state called ‘parasitic currents’ were often observed to be considerable due to the imbalance between the interface tension force and pressure gradients near the interface [40,41]. This is because the interface in these tests covers several cells (in mesh based method) or particle layers (in meshless method) within which curvature and surface tension are smeared. The transitional curvature and pressure do not strictly satisfy the interface conditions stated by Eq. (4), leading to relatively high parasitic currents when the droplet reaches its equilibrium state. In fact, even with sharp pressure jump based on a fix grid method [41], the tested drop in static equilibrium can still have a considerable velocity magnitude, which was likely caused by the inaccurate curvature estimation on fixed grid.

With the newly developed implementation for the surface tension, sharp pressure jump across a single interface particle layer is achieved and curvature is accurately estimated through locally fitting the interface particles. The test follows the settings in Hoang et al. [36] and all the parameters are non-dimensionalized giving the density of $\rho_2 = 3546$, the viscosity of $\mu_2 = 1.0$, the density ratio of $\rho_2/\rho_1 = 2$, the viscosity ratio of $\mu_2/\mu_1 = 0.4$ and the interface tension of $\sigma = 1.0$. The domain size is $L_2 = 2L_1 = 4$. When the inner drop reaches its equilibrium state, the shape is transformed to a circle remaining the same area as the initial square. According to Laplace law, the pressure inside and outside the circle are two constants having a jump at the circle. By plotting the pressure on $y = 2.0$ within the right half side of the square, i.e. $2.0 \leq x \leq 4.0$, Fig. 3 illustrates a higher constant pressure inside the inner circle and a lower constant outside the circle with the transition between two constants completed on one interface particle. One can also observe that the simulations using 40, 60 and 80 particles along the outside square edge (giving the particle distance of 0.025, 0.017 and 0.013 respectively) largely provide similar results which are close to the analytical solution. From the enlarged insert in Fig. 3, well convergence can be observed when the number of particles increases. The reason for such sharp pressure jump lies in the newly proposed Eqs. (20) and (21) which strictly satisfy the pressure jump condition by storing two pressure values for individual phases on one interface particle. Similar simulations were also conducted by the SPH in Zainali et al. [20], by treating the interface force continuously as in the CSF method. Although the accuracy of interface force was improved by testing various kernel combinations for the governing equations and the interface force, the pressure still shows gradual reduction across the interface accompanied by slight oscillations somewhat losing the sharp pressure jump as stated in Laplace law. Pressure snapshots of t =6, 30 and 300 are demonstrated in Fig. 4 with interface particles marked black, illustrating the pressure fields which drive the shape oscillates (i.e. (a) and (b)) until the equilibrium state (i.e. (c)). The volume conservation issue of particle based methods simulating incompressible flow was discussed by Nair and Tomar [42]. In this case, the volume conservation can be validated by the occupied area of the inner fluid after long time simulation as it becomes circular at equilibrium. In Fig. 3, the position of the pressure jump of the Laplace law is based on the radius of the final circle whose area equals to that of the initial square of $L_1 \times L_1$. The matched location of the pressure jump between the simulation and the Laplace law illustrates the area conservation during shape transformation.

By recording the maximum velocity in the whole domain, Fig. 5 shows that after long time simulation, the drop reaches its equilibrium and due to the energy dissipation of viscosity the maximum velocity is gradually reduced and becomes a stable but non-zero value which is caused by numerical errors and called the parasitic current. By checking the maximum velocity dissipation, not only the convergence is achieved when 80 particles are used, the spurious current is also significantly reduced and stabilized by the new interface tension implementation compared to conventional CSF model [36].

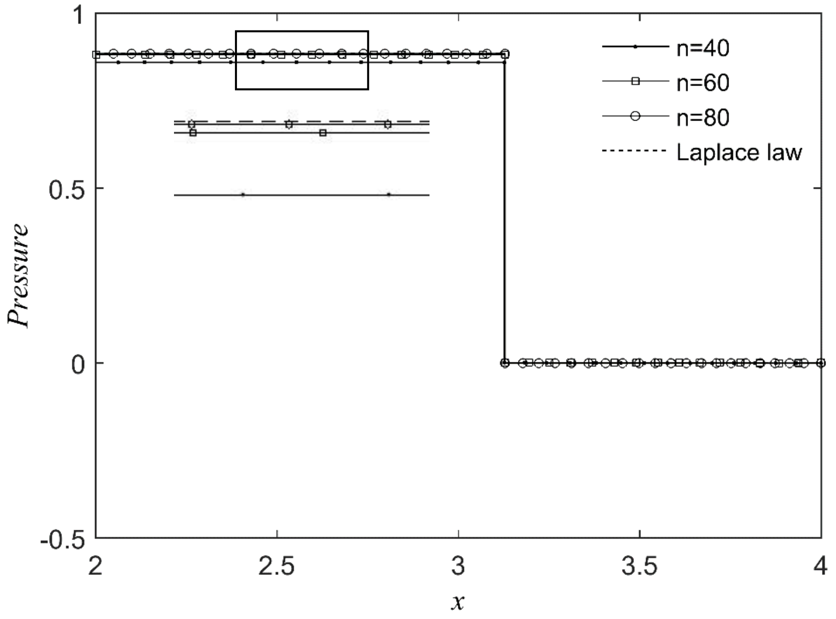

Fig. 3: Pressures inside and outside the equilibrium droplet at y=2.0 for different particle numbers.

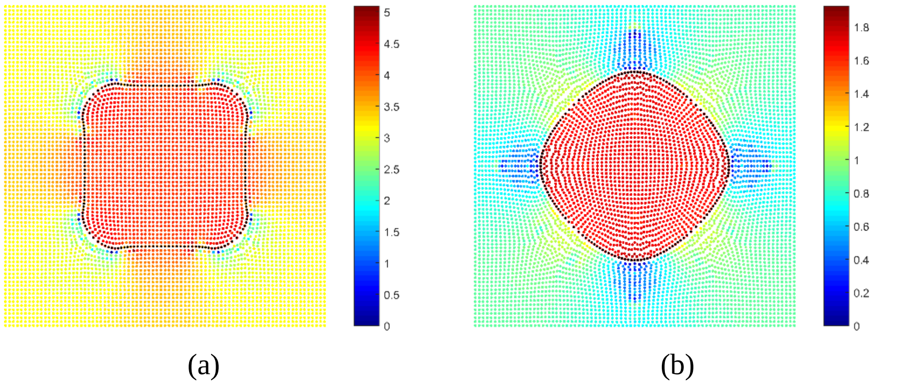

(a)

(b)

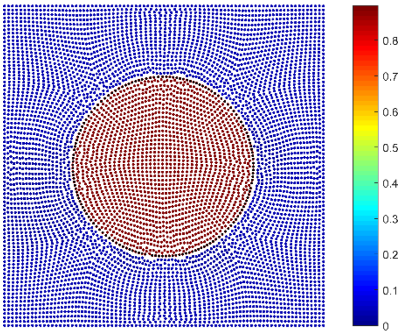

(c)

Fig. 4: Pressure snapshots during droplet oscillation at time instants of 6 (a), 30 (b) and 300 (c).

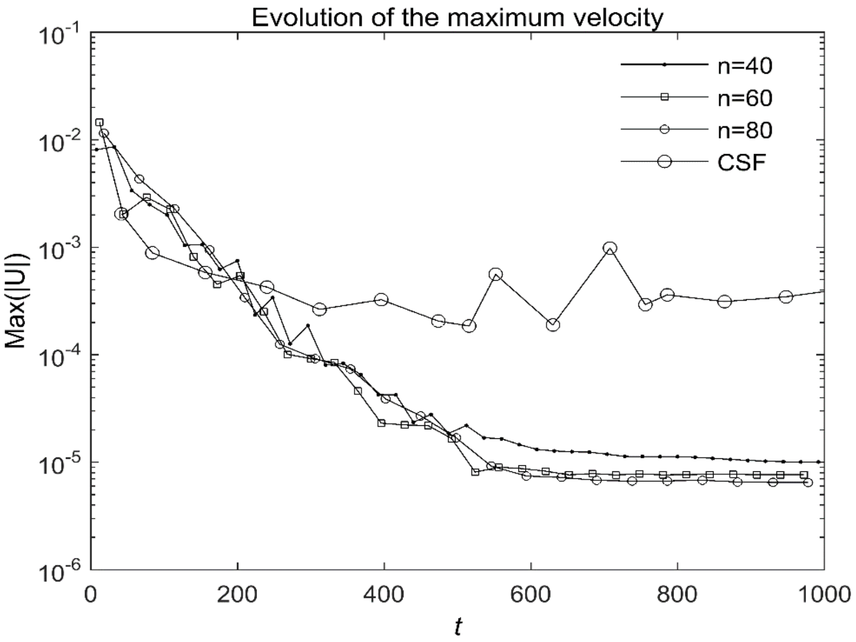

Fig. 5: Time histories of maximum velocity with different particle numbers along the outside square edge. The large circle solid line is from Hoang et al. [36] adopting CSF model with cell number of 100.

4.2 Capillary wave

The capillary wave is a surface tension driven flow and its amplitude damping oscillation is often used as a benchmark to test the accuracy of numerical schemes for viscous, surface tension driven two-phase flows [1,41]. In this section, the proposed pressure formulations, Eqs. (20) and (21), that include the effects of high viscosity and interface tension, will be validated and the differences between the results from the use of Eq. (14) and that for low viscous stress will also be shown.

A computational domain of $H \times H$ is equally split into two sections filled by two fluids with identical kinematical viscosity. An initial sinusoidal perturbation is applied to the interface with the amplitude of $a_0 = 0.01H$ and the wave length of H. The analytical solution of this initial value problem for the linearized case was found by Prosperetti [43]. Due to infinite domains used in Prosperetti's theory, periodic boundary is applied on the wave progressing direction. To simulate such boundary, three columns of particles are added on the left and right hand sides out of the domain. The added particles on the right hand side carry the information, i.e., density, viscosity, pressure and velocity, of three columns of particles on the far left of computational domain and vice versa. Following Wang and Tong [41], we set the wave length $\lambda = H = 1m$, the dynamic viscosity $\mu_l = \mu_k = 1.0P_a \cdot s$, the density $\rho_l = \rho_k = 100kg/m^3$ and the interfacial tension coefficient $\sigma = 30N/m$. The Ohnesorge number is $Oh = \frac{\mu}{\sqrt{(\sigma\rho\lambda)}} = 1/\sqrt{3000}$. Convergence tests of different particle distance are first carried out and the wave amplitudes with different particle numbers in a wave length are shown in Fig. 6(a), in which $\omega_0 = \sqrt{\sigma k^3/(\rho_l + \rho_k)}$ and k is the wave number. Results of another test with the same parameters but a higher viscosity of $0.05\mathrm{m}^2/\mathrm{s}$ are shown in Fig. 6(b), in which a stronger damping can be observed. For both cases, 64 nodes in a wave length are sufficient to achieve a convergent results and this number will be applied to the following capillary wave cases unless stated otherwise. To observe the convergent rate, L_2 norm is calculated as $L_2 = \sqrt{\frac{1}{N}\sum_{i=1}^{N}(a_i - a_{exact})^2}$, where N is the number of results on time history, a_i is the amplitude from numerical simulation and a_{exact} is from Prosperetti's analytical solution. For both viscosities of $0.01\mathrm{m}^2/\mathrm{s}$ and $0.05\mathrm{m}^2/\mathrm{s}$, values of L_2 are calculated for different particle numbers per wave length of 16, 32, 64 and 128. Fig. 7 plots the errors with respect to particle numbers, showing approximate second order convergent rate for both viscosities. The pressure fields at two time instants are shown by the left column of Fig. 8 illustrating smooth pressure distributions within each phase and sharp jumps at the interface caused by the interface tension and normal viscous stress. The right column of the Fig. 8 shows the corresponding velocity fields which are continuous at the interfaces as indicated by black dots.

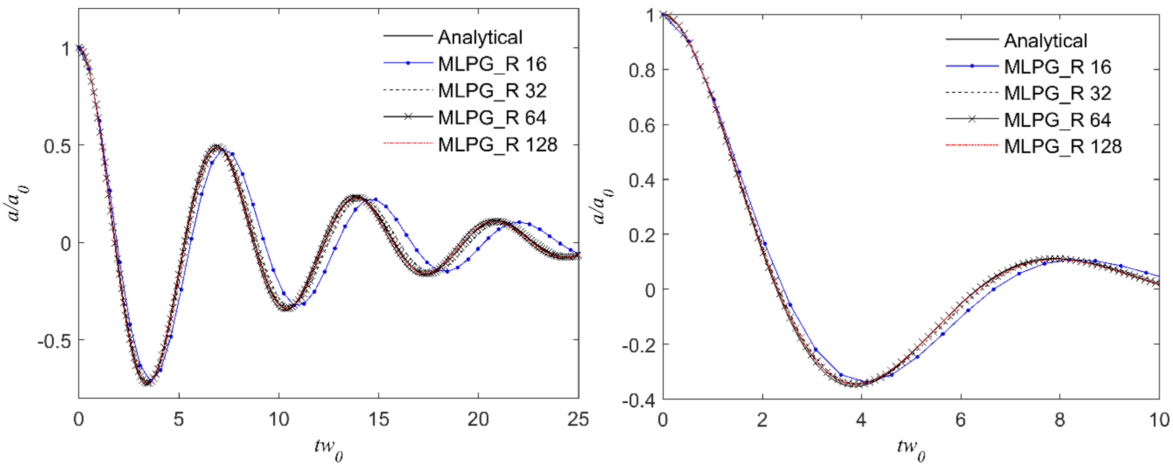

(a) (b)

Fig. 6: Amplitude time history with different particle numbers per wave length. Kinematic viscosities are $0.01m^2/s$ in (a) and $0.05m^2/s$ in (b).

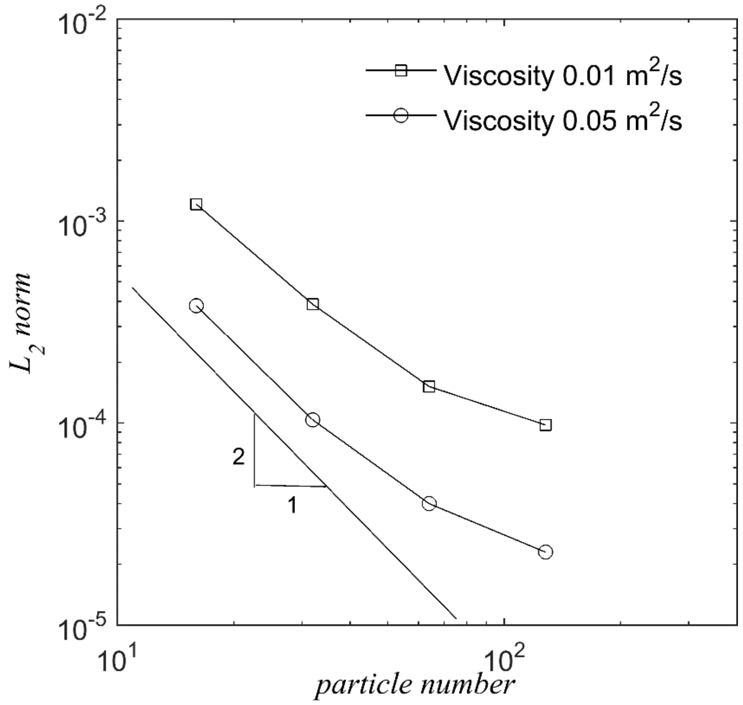

Fig. 7: L_2 norms of particle number of 16, 32, 64 and 128 per wave length for the viscosities of $0.01m^2/s$ and $0.05m^2/s$. The solid line indicates the second order convergence.

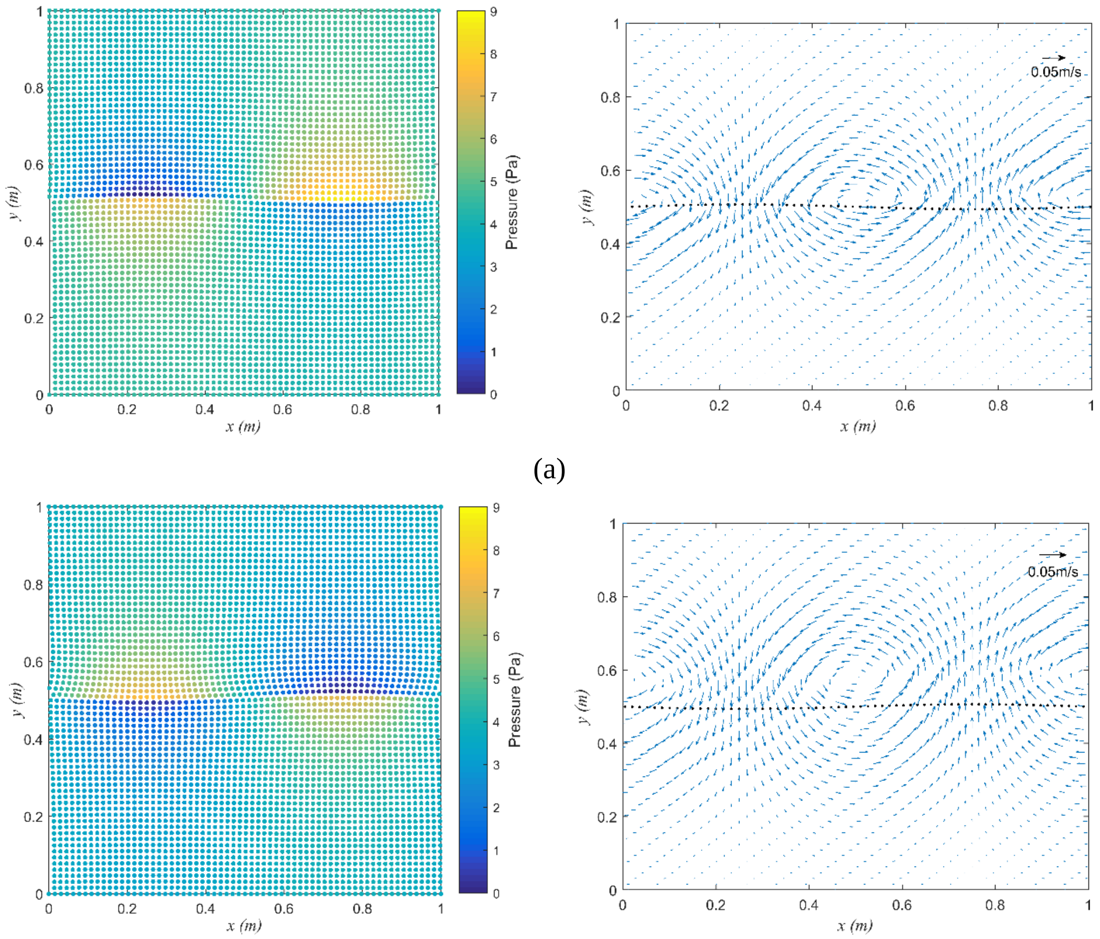

(a)

(b)

Fig. 8: Pressure and velocity fields at $t\omega_0 = 1.0$ (a) and $t\omega_0 = 2.9$ (b), respectively. The black dots in velocity fields denote the location of the interface.

For comparisons between $\left[\frac{\nabla p}{\rho}\right]_{HV}$ and $\left[\frac{\nabla p}{\rho}\right]_{LV}$, the viscosities of $0.001\text{m}^2/\text{s}$ and $0.01\text{m}^2/\text{s}$ are first tested, giving the wave amplitudes shown in Fig. 9(a) and (b). Results with both conditions almost coincide and agree well with the analytical solution. But for the higher viscosities of $0.05\text{m}^2/\text{s}$ and $0.075\text{m}^2/\text{s}$, the differences in the results obtained by the two conditions increased considerably as shown in Fig. 9(c) and (d), indicating that the results obtained with the jump formulation considering high viscous effects (i.e., $\left[\frac{\nabla p}{\rho}\right]_{HV}$) can match the analytical solution much better than that with the assumption of small viscous effects (i.e., $\left[\frac{\nabla p}{\rho}\right]_{LV}$). The relative error of the amplitude, defined as $E_{r,i} = |a_i - a_{exact,i}|/|a_{exact,i}|$, can be well over 100% at certain phases when $\left[\frac{\nabla p}{\rho}\right]_{LV}$ is used. These results demonstrate clearly that $\left[\frac{\nabla p}{\rho}\right]_{HV}$ covers the range of both low and high viscosity whereas $\left[\frac{\nabla p}{\rho}\right]_{LV}$ only works well with low viscosity flows. Comparisons of full interface profiles at two time instants for each viscosity, i.e. $t\omega_0$ = 5.7 and 6.4 for 0.05m^2/s as well as $t\omega_0$ =5.7 and 7.6 for 0.075m^2/s, are illustrated in Fig. 10, further showing the difference by adopting $\left[\frac{\nabla p}{\rho}\right]_{HV}$ and$\left[\frac{\nabla p}{\rho}\right]_{LV}$.

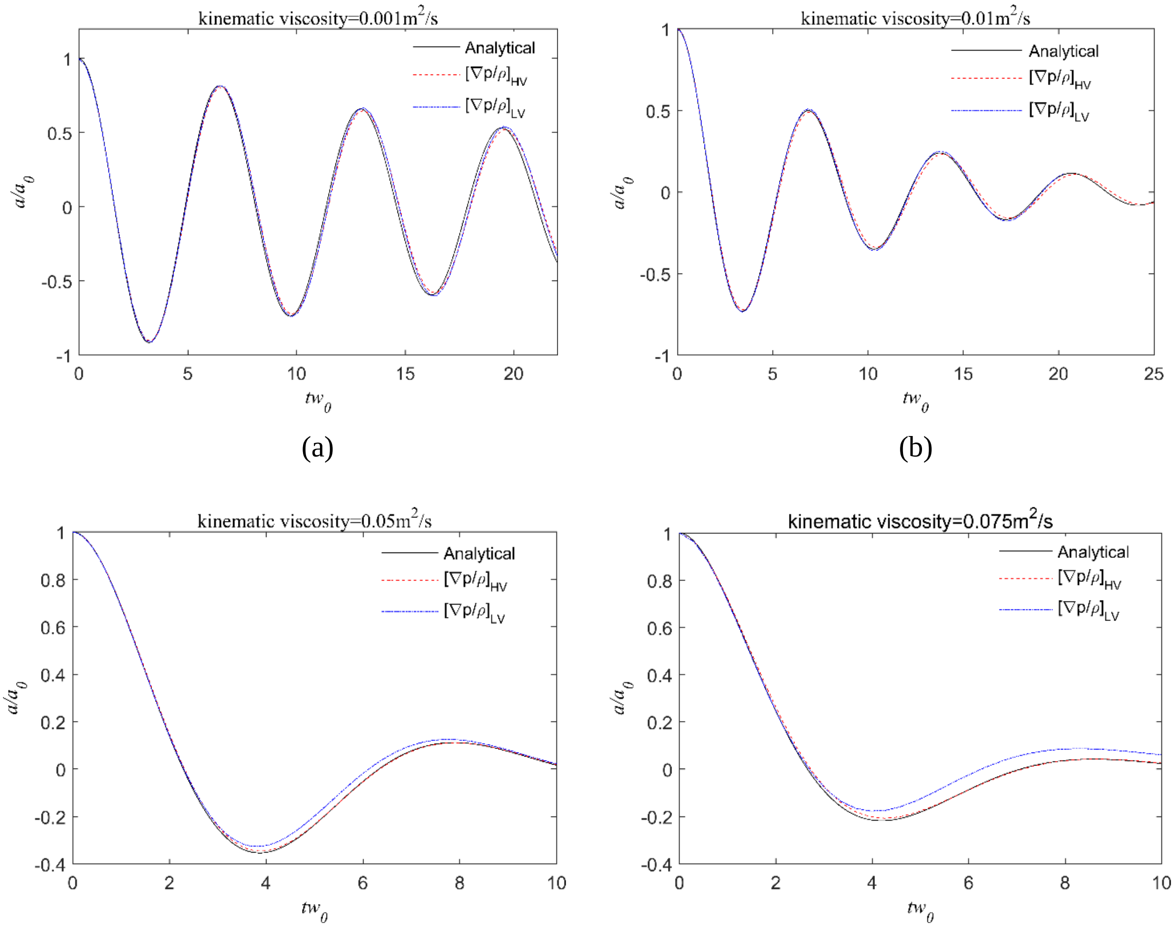

(a)

(b)

(c)

(d)

Fig. 9: Comparisons of amplitude time history predicted with the two jump conditions of $\nabla p/\rho$, respectively for viscosities of 0.001, 0.01, 0.05and 0.075m^2/s.

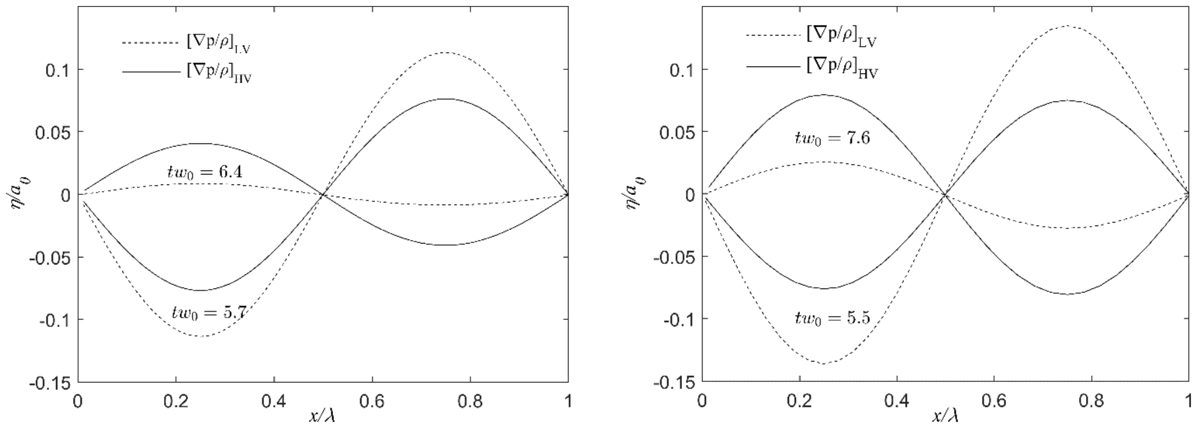

(a) (b)

Fig. 10: Comparisons of interface profiles predicted with two jump conditions of $\nabla p/\rho$ at $t\omega_0 = 5.7$ and 6.4 for the viscosity of $0.05 m^2/s$ in (a) and at $t\omega_0$ =5.5 and 7.6 for the viscosity of $0.075 m^2/s$ in (b).

4.3 Bubble rising

In this section the newly proposed interface treatment with MLPG_R method is further tested and validated against the published results related to bubble rising in viscous fluids which is strongly affected by fluid viscosity and the surface tension and has been widely adopted to exam the accuracy of surface tension and viscous terms estimation in terms of predicted bubble shapes and rising velocities [20,22].

Based on the definition in Hysing et al. [44], a two dimensional computational domain with $H/B = 2/1$ is adopted with the slip condition being imposed at the left and right walls and non-slip boundary at the top and bottom walls, as shown in Fig. 11. A bubble with the radius of $R = 0.25$ is initially set at $\left(\frac{B}{2}, 2R\right)$ where $B = 4R$. Non-dimensional densities assigned to fluids inside and outside the bubble are $\rho_k = 100$ and $\rho_l = 1000$, respectively. The viscosities are $\mu_k = 1$ and $\mu_l = 10$ and the interface tension coefficient is $\sigma = 24.5$.

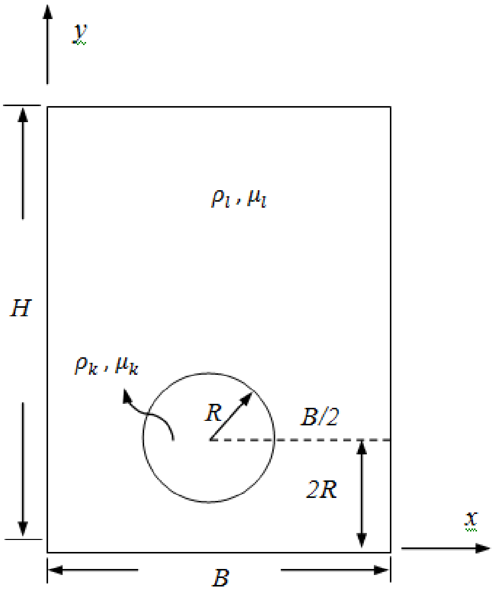

Fig. 11: The setup of the bubble rising case

During bubble rising and shape translation, the centroid position of the bubble, $\vec{x}_c$, and velocity, $\vec{u}_c$,may be used to track the bubble movement [43,44] and are determined as

$$\vec{x}_c = \frac{\int_\Omega \vec{x} d\Omega}{\int_\Omega 1 d\Omega} \text{ and } \vec{u}_c = \frac{\int_\Omega \vec{u} d\Omega}{\int_\Omega 1 d\Omega}$$

where Ω is the domain occupied by the bubble. The simulations of this case are conducted with three initial particle distances of $dl = 1/[80, 120,160]$ to the nondimensional time $t = 3$. Apart from the benchmark results from Hysing et al. [44] in which centroid positions and rising velocities were obtained by FEM with the interface captured by level set algorithm and the results from FVM using Volume of Fluid (VOF) capturing algorithm conducted in OpenFOAM solver (open source CFD) are also presented.

Fig. 12(a) compares the rising velocity from the two-phase MLPG_R method with particle distances of 1/40, 1/60 and 1/80, FEM of finest grids of 1/320 given by Hysing et al. [44] and FVM with refined and converged grids of 1/240 given by the OpenFOAM. The solutions from MLPG_R with different particle distances are close to each other but still have a noticeable deviation compared with Hysing et al.'s benchmark results. It can also be observed that the velocity converges when the distance is decreased to be 1/80 and this converged velocity locates between solutions of FEM and

FVM. Compared to OpenFOAM's solution, the results obtained by multiphase MLPG_R are closer to the benchmark, probably due to the reduction in spurious currents which was previously discussed in square-droplet case. Fig. 12(b) illustrates the time histories of bubble centroid position as predicted by MLPG_R using different particle distances, FVM and FEM with fine grids. Similar to the rising velocity, good results are obtained by these three MLPG_R resolutions which are located between that of FVM and FEM.

According to numerical tests of MLPG_R, the bubble gets deformed during rising. But it stays compact as one enclosed region throughout the simulation which is caused by the strong influence of the surface tension. The shape of the bubble finally becomes stable and the terminal shapes at t=3 obtained by different particle distances are shown in Fig. 13. The shape also converges at $dl = 1/80$ for MLPG_R method and largely agrees with those from FEM by Level set method [44] and FVM by VOF using OpenFOAM.

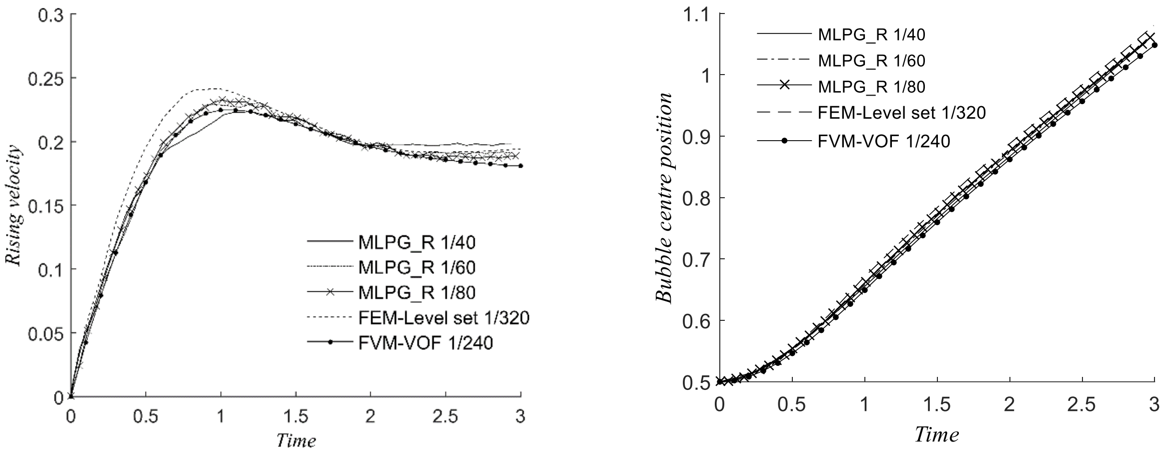

(a) (b)

Fig. 12: Rising velocities (a) and centroid position of the bubble (b) from MLPG_R method with initial particle distance of 1/40, 1/60 and 1/80, FEM-Level set method [44] and FVM-VOF (OpenFOAM) with very fine grids.

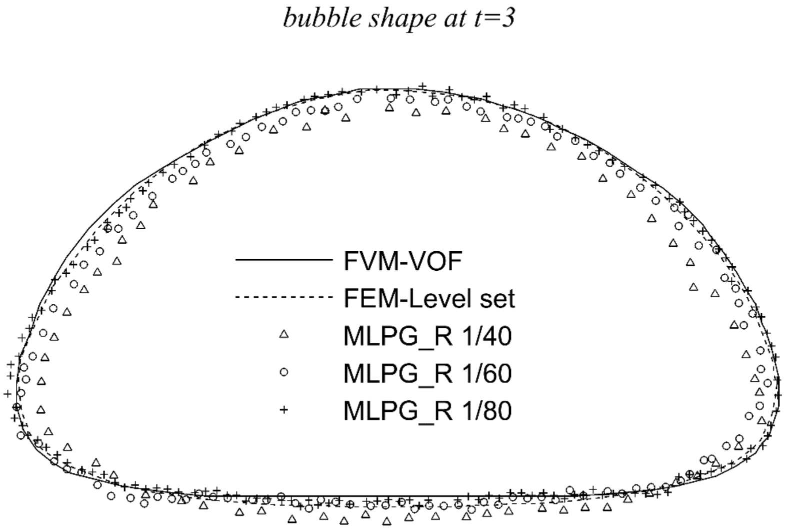

Fig. 13: Bubble shape at t=3 from the MLPG_R method with initial particle distance of 1/40, 1/60 and 1/80, FEM-Level set method [44] and FVM-VOF (OpenFoam) with very fine mesh.

4.4 Rayleigh-Taylor instability

Rayleigh-Taylor instability typically occurs in multiphase flows with complex interface profiles characterised by significant distortions of particle distribution in long time simulation. The test chosen in this paper involves two immiscible fluids with density of the upper phase being $\rho_k = 1.8$ and the lower phase $\rho_l = 1.0$ which are enclosed in a rectangular domain with the length of $L = 1$ and the depth of $2L$. The phases are initially separated by $y/L = 1 - 0.15\sin(2\pi x/L)$. The Reynolds number based on the reference velocity $u_{ref} = \sqrt{gL}$ is $R_e = u_{ref}L/\upsilon = 420$ where υ is the kinematic viscosity.

The simulation was performed with 60×120 particles, resulting in an initial distance of 1/60. Fig. 14 illustrates phase configurations at t=1, 3 and 5 (nondimensionalized by the time scale of $\sqrt{L/g}$) compared with the results of [22] using particle distance of 1/256. A good agreement is achieved for the growth of the instability even when the interface is highly complex. Without any artificial treatments to sharpen the interface such as adding different types of repulsion forces between phases [22,45,46] which is widely adopted by particle based methods, this algorithm achieves clear separation of two phases by implementing the conditions in Eqs. (20) and (21) which enforces the balance of the stress and the continuity of the velocity at the interface.

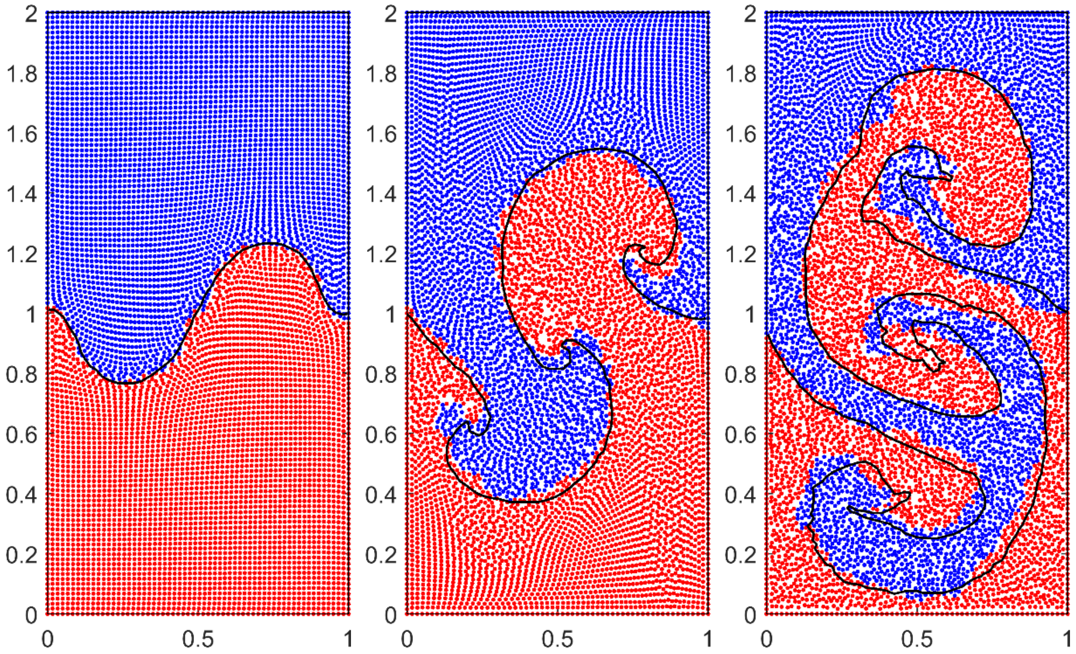

(a) (b) (c)

Fig. 14: Phase configurations of the Rayleigh-Taylor instability at t=1, t=3 and t=5 as shown in (a), (b) and (c) by blue and red dots. Black curves are the results of the interfaces from [22].

5. Conclusion

In this work, a new interface treatment technique for multi-phase meshless methods considering interface tension and high viscosity is proposed and is incorporated into the MLPG_R method to simulate two-phase flows. The interface conditions imposed are the stress balance including interface tension in the normal direction of the interface and the velocity continuity at the interface. Based on these interface conditions, jumps in the pressure and in the ratio of pressure gradient to the density are derived. The curvature of the interface is determined from the local reconstructed interface curve which is fitted by MLS approach. The new two-phase model has been validated with analytical solutions for square-droplet deformation and capillary waves. The simulation obtains a precise and discontinuous pressure at the interface with depressed parasitic current and demonstrates the capability of the model in handling high viscosity showing approximate second order convergent rate of the solution method. The simulation of the bubble rising shows acceptable agreement with other numerical models which further validates the new model's capability in dealing with two-phase flow problems involving high viscosity and interface tension. The Rayleigh-Taylor instability case demonstrates the capacity of the model for dealing with complex interface profiles and maintaining clear separations of two phases. It should be noted that although the proposed interface treatment technique is implemented based on MLPG_R method in this work, it is straightforward to apply it to other meshless methods as long as interface particles are clearly identified.

Appendix

To ensure a one-valued interface curve, a local coordinate system is first built (as shown in Fig. A1) with the new origin O' being at the averaged coordinates of neighbouring interface particles, i.e., interface particles within the circle in Fig. A1, and the y' axis pointing to the concerned particle. Secondly a local curve of the concerned particle will be constructed. Unlike the polynomial interpolation used by Zhang et al. [28], the second-order MLS technique is used to ensure a smooth curve even with irregularly distributed interface particles. Details of MLS technique can be found in Ma [29] and here only the curve reconstruction procedures are described.

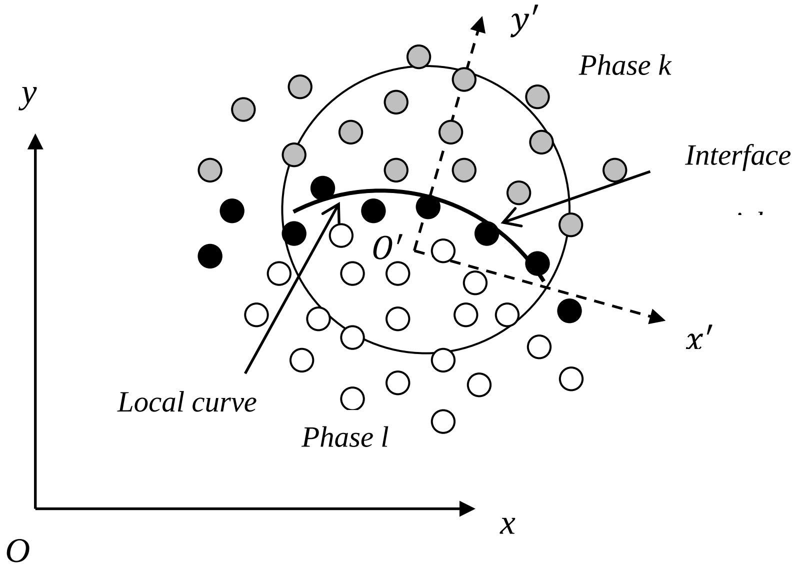

Fig. A1: Coordinate transformation for local curve construction.

To obtain a second-order curve in $x'o'y'$ system, the approximant $y'^h(x')$ of $y'(x')$ having x' within the support domain, can be defined by

$$y'^h(x') = \boldsymbol{p}^T(x')\boldsymbol{a}(x')$$

where $P^T(x')$ is a complete monomial basis of order m which can be written as

$$\boldsymbol{p}^T(x') = [1, x', x'^2]\,, \quad m = 3$$

and $\boldsymbol{a}(x')$ is a vector containing coefficients $a_j(x'), j = 1,2, \dots, m$ and can be expressed as

$$\boldsymbol{a}(x') = \boldsymbol{A}^{-1}(x')\boldsymbol{B}(x')\boldsymbol{y}'$$

where $\boldsymbol{y}'^T = [y'_1, y'_2, \dots, y'_n]$ and $y'_i, i = 1,2, \dots, n$ are the y' values of surrounding interface particles in the support domain. The matrices $\boldsymbol{A}(x')$ and $\boldsymbol{B}(x')$ are defined as

$$\boldsymbol{A}(x') = \boldsymbol{P}^T\boldsymbol{W}\boldsymbol{P} = \sum_{\mathrm{i}=1}^{\mathrm{n}} \mathrm{w_i}(x')\,\boldsymbol{p}(x'_i)\boldsymbol{p}^T(x'_i)$$

$$\boldsymbol{B}(x') = \boldsymbol{P}^T\boldsymbol{W} = [\mathrm{w_1}(x')\boldsymbol{p}(x'_1), \mathrm{w_2}(x')\boldsymbol{p}(x'_2), \dots, \mathrm{w_n}(x')\boldsymbol{p}(x'_n)]$$

where the matrices $\boldsymbol{P}$ and $\boldsymbol{W}$ are defined as

$$\boldsymbol{P} = \begin{bmatrix} \boldsymbol{p}^T(x'_1) \\ \boldsymbol{p}^T(x'_2) \\ \cdots \\ \boldsymbol{p}^T(x'_n) \end{bmatrix}, \boldsymbol{W} = \begin{bmatrix} \mathrm{w_1}(x') & \cdots & \boldsymbol{0} \\ \cdots & \cdots & \cdots \\ \boldsymbol{0} & \cdots & \mathrm{w_n}(x') \end{bmatrix}$$

Upon solving $\boldsymbol{a}(x')$, the interpolated curve can be expressed as

$$y'^h(x') = a_1(x') + a_2(x')x' + a_3(x')x'^2$$

The curvature and the normal vector of the interface are subsequently calculated from the interpolated curve. The curvature κ is given by

$$\kappa = \frac{\left|d^2y'^h/dx'^2\right|}{[1 + (dy'^h/dx')^2]^{3/2}}$$

The normal vector in the local coordinate system is taken as

$$\vec{n}' = \begin{cases} \left(\dfrac{dy'^h}{dx'}, -1\right), & \text{for } d^2y'^h/dx'^2 < 0 \\ \left(-\dfrac{dy'^h}{dx'}, 1\right), & \text{for } d^2y'^h/dx'^2 > 0 \end{cases}$$

It should be noted that the curvature is not affected by the transformation of the coordinate system but the normal vector calculated with respect to the local coordinate system needs to be converted back to the original fixed xoy system.

Acknowledgements

Support from EPSRC grant EP/N006569/1 is gratefully acknowledged. The author wishes to thank Prof. Qingwei Ma from City University London for his invaluable comments on the present paper.

References

[1] S. Popinet, ‘An accurate adaptive solver for surface-tension-driven interfacial flows’, *J. Comput. Phys.*, vol. 228, no. 16, pp. 5838–5866, 2009.

[2] X. Y. Hu and N. a. Adams, ‘A multi-phase SPH method for macroscopic and mesoscopic flows’, *J. Comput. Phys.*, vol. 213, no. 2, pp. 844–861, 2006.

[3] M. Rudman, ‘Volume-Tracking Methods for Interfacial Flow Calculations’, *Int. J. Numer. Methods Fluids*, vol. 24, no. 7, pp. 671–691, 1997.

[4] F. Xiao, Y. Honma, and T. Kono, ‘A simple algebraic interface capturing scheme using hyperbolic tangent function’, *Int. J. Numer. Methods Fluids*, vol. 48, no. 9, pp. 1023–1040, 2005.

[5] M. Sussman, P. Smereka, and S. Osher, ‘A Level Set Approach for Computing Solutions to Incompressible Two-Phase Flow’, *J. Comput. Phys.*, vol. 114, pp. 146–159, 1994.

[6] S. Osher and R. P. Fedkiw, ‘Level Set Methods: An Overview and Some Recent Results’, *J. Comput. Phys.*, vol. 169, no. 2, pp. 463–502, 2001.

[7] J. U. Brackbill, D. B. Kothe, and C. Zemach, ‘A continuum method for modeling surface tension’, *J. Comput. Phys.*, vol. 100, pp. 335–354, 1992.

[8] M. Wörner, ‘Numerical modeling of multiphase flows in microfluidics and micro process engineering: A review of methods and applications’, *Microfluid. Nanofluidics*, vol. 12, no. 6, pp. 841–886, 2012.

[9] R. R. Nourgaliev, M. S. Liou, and T. G. Theofanous, ‘Numerical prediction of interfacial instabilities: Sharp interface method (SIM)’, *J. Comput. Phys.*, vol. 227, no. 8, pp. 3940–3970, 2008.

[10] M. Sussman, K. M. Smith, M. Y. Hussaini, M. Ohta, and R. Zhi-Wei, ‘A sharp interface method for incompressible two-phase flows’, *J. Comput. Phys.*, vol. 221, no. 2, pp. 469–505, 2007.

[11] R. P. Fedkiw, T. Aslam, B. Merriman, and S. Osher, ‘A Non-oscillatory Eulerian Approach to Interfaces in Multimaterial Flows (the Ghost Fluid Method)’, *J. Comput. Phys.*, vol. 152, no. 2, pp. 457–492, 1999.

[12] J. Luo, X. Y. Hu, and N. a. Adams, ‘A conservative sharp interface method for incompressible multiphase flows’, *J. Comput. Phys.*, vol. 284, pp. 547–565, 2015.

[13] Z. Tukovic and H. Jasak, ‘A moving mesh finite volume interface tracking method for surface tension dominated interfacial fluid flow’, *Comput. Fluids*, vol. 55, pp. 70–84, 2012.

[14] X. Y. Hu and N. A. Adams, ‘An incompressible multi-phase SPH method’, *J. Comput. Phys.*, vol. 227, no. 1, pp. 264–278, 2007.

[15] A. M. Tartakovsky, K. F. Ferris, and P. Meakin, ‘Lagrangian particle model for multiphase flows’, *Comput. Phys. Commun.*, vol. 180, no. 10, pp. 1874–1881, 2009.

[16] A. Khayyer, H. Gotoh, and S. D. Shao, ‘Enhanced predictions of wave impact pressure by improved incompressible SPH methods’, *Appl. Ocean Res.*, vol. 31, no. 2, pp. 111–131, 2009.

[17] A. Zhang, P. Sun, and F. Ming, ‘An SPH modeling of bubble rising and coalescing in three dimensions’, *Comput. Methods Appl. Mech. Eng.*, vol. 294, no. 145, pp. 189–209, 2015.

[18] A. Shakibaeinia and Y. Jin, ‘MPS mesh-free particle method for multiphase flows’, *Comput. Methods Appl. Mech. Eng.*, vol. 229–232, pp. 13–26, 2012.

[19] A. Khayyer and H. Gotoh, ‘Enhancement of performance and stability of MPS mesh-free particle method for multiphase flows characterized by high density ratios’, *J. Comput. Phys.*, vol. 242, pp. 211–233, 2013.

[20] A. Zainali, N. Tofighi, M. S. Shadloo, and M. Yildiz, ‘Numerical investigation of Newtonian and non-Newtonian multiphase flows using ISPH method’, *Comput. Methods Appl. Mech. Eng.*, vol. 254, pp. 99–113, 2013.

[21] M. Zhang, ‘Simulation of surface tension in 2D and 3D with smoothed particle hydrodynamics method’, *J. Comput. Phys.*, vol. 229, no. 19, pp. 7238–7259, 2010.

[22] K. Szewc, J. Pozorski, and J. P. Minier, ‘Spurious interface fragmentation in multiphase SPH’, *Int. J. Numer. Methods Eng.*, vol. 103, no. 9, pp. 625–649, 2015.

[23] S. D. Shao, ‘Incompressible smoothed particle hydrodynamics simulation of multifluid flows’, *Int. J. Numer. Methods Fluids*, vol. 69, pp. 1715–1735, 2012.

[24] Y. Zhou, Q. W. Ma, and S. Yan, ‘MLPG_R method for modelling 2D flows of two immiscible fluids without considering surface tension’, *Int. J. Numer. Methods Fluids*. Accepted

[25] S. J. Lind, P. K. Stansby, and B. D. Rogers, ‘Incompressible–compressible flows with a transient discontinuous interface using smoothed particle hydrodynamics (SPH)’, *J. Comput. Phys.*, vol. 309, pp. 129–147, 2016.

[26] J. J. Monaghan, ‘Simulating surface tension with smoothed particle hydrodynamics’, *Int. J. Numer. Methods Fluids*, vol. 33, no. 3, pp. 333–353, 2000.

[27] S. Adami, X. Y. Hu, and N. A. Adams, ‘A new surface-tension formulation for multi-phase SPH using a reproducing divergence approximation’, *J. Comput. Phys.*, vol. 229, no. 13, pp. 5011–5021, 2010.

[28] M. Zhang, S. Zhang, H. Zhang, and L. Zheng, ‘Simulation of surface-tension-driven interfacial flow with smoothed particle hydrodynamics method’, *Comput. Fluids*, vol. 59, pp. 61–71, 2012.

[29] Q. W. Ma, ‘MLPG Method Based on Rankine Source Solution for Simulating Nonlinear Water Waves’, *C. - Comput. Model. Eng. Sci.*, vol. 9, no. 2, pp. 193–209, 2005.

[30] S. D. Shao and E. Y. M. Lo, ‘Incompressible SPH method for simulating Newtonian and non-Newtonian flows with a free surface’, *Adv. Water Resour.*, vol. 26, no. 7, pp. 787–800, 2003.

[31] Q. W. Ma, ‘Meshless local Petrov-Galerkin method for two-dimensional nonlinear water wave problems’, *J. Comput. Phys.*, vol. 205, no. 2, pp. 611–625, 2005.

[32] S. Koshizuka and Y. Oka, ‘Moving-particle semi-implicit method for fragmentation of incompressible fluid’, *Nuclear science and engineering*, vol. 123, no. 3. pp. 421–434, 1996.

[33] Q. W. Ma and J. T. Zhou, ‘MLPG_R Method for Numerical Simulation of 2D BreakingWaves’, *C. - Comput. Model. Eng. Sci.*, vol. 43, no. 3, pp. 277–303, 2009.

[34] M. Kang, R. P. Fedkiw, and X. D. Liu, ‘A boundary condition capturing method for

multiphase incompressible flow', *J. Sci. Comput.*, vol. 15, no. 3, pp. 323–360, 2000.

[35] Y. Zhou and Q. W. Ma, 'A New Interface Identification Technique Based on Absolute Density Gradient for Violent Flows', *C. - Comput. Model. Eng. Sci.*, 2016. In press

[36] D. A. Hoang, V. van Steijn, L. M. Portela, M. T. Kreutzer, and C. R. Kleijn, 'Benchmark numerical simulations of segmented two-phase flows in microchannels using the Volume of Fluid method', *Comput. Fluids*, vol. 86, pp. 28–36, 2013.

[37] O. Desjardins, V. Moureau, and H. Pitsch, 'An accurate conservative level set/ghost fluid method for simulating turbulent atomization', *J. Comput. Phys.*, vol. 227, no. 18, pp. 8395–8416, 2008.

[38] M. Owkes and O. Desjardins, 'A mesh-decoupled height function method for computing interface curvature', *J. Comput. Phys.*, vol. 281, pp. 285–300, 2015.

[39] L. D. Landau and E. M. Lifshitz, *Fluid Mechanics*, 2nd ed., vol. 6. Oxford: cambridge university press, 1987.

[40] S. Shin, S. I. Abdel-Khalik, V. Daru, and D. Juric, 'Accurate representation of surface tension using the level contour reconstruction method', *J. Comput. Phys.*, vol. 203, no. 2, pp. 493–516, 2005.

[41] Z. Wang and A. Y. Tong, 'A sharp surface tension modeling method for two-phase incompressible interfacial flows', *Int. J. Numer. Methods Fluids*, no. 64, pp. 709–732, 2010.

[42] P. Nair and G. Tomar, 'Volume conservation issues in incompressible smoothed particle hydrodynamics', *J. Comput. Phys.*, vol. 297, pp. 689–699, 2015.

[43] A. Prosperetti, 'Motion of two superposed viscous fluids', *Phys. fluids*, vol. 24, no. 7, pp. 1217–1223, 1981.

[44] S. Hysing, S. Turek, D. Kuzmin, N. Parolini, E. Burman, and S. Ganesan, 'Quantitative benchmark computations of two-dimensional bubble dynamics', *Int. J. Numer. Methods Fluids*, no. 60, pp. 1259–1288, 2009.

[45] T. Chen, P. D. Minev, and K. Nandakumar, 'A projection scheme for incompressible multiphase flow using adaptive Eulerian grid: 3D validation', *Int. J. Numer. Methods Fluids*, vol. 48, no. 4, pp. 455–466, 2005.

[46] A. Colagrossi and M. Landrini, 'Numerical simulation of interfacial flows by smoothed particle hydrodynamics', *J. Comput. Phys.*, vol. 191, no. 2, pp. 448–475, 2003.

[47] N. Grenier, M. Antuono, a. Colagrossi, D. Le Touzé, and B. Alessandrini, 'An Hamiltonian interface SPH formulation for multi-fluid and free surface flows', *J. Comput. Phys.*, vol. 228,

no. 22, pp. 8380–8393, 2009.